Interpretation of D_α video diagnostics data as a contribution to plasma edge characterisation

J Harhausen‡, A Kallenbach, C Fuchs and the ASDEX Upgrade Team

Max-Planck-Institut für Plasmaphysik, EURATOM Association, D-85748 Garching, Germany

E-mail: harhausen@inp-greifswald.de, arne.kallenbach@ipp.mpg.de

Abstract. The spatial distribution of the neutral source profile is an important quantity for the understanding of the pedestal density profile and effects like its influence on rotational shear by momentum exhange. Analytic models as well as numerical predictive codes require experimental data on the magnitude and poloidal distribution of the neutral flux density in order to be validated. This paper describes the measurement and interpretation of D_α radiance data obtained with a pair of tangentially viewing cameras at the ASDEX Upgrade tokamak. Reflection at the tungsten tile surfaces covering most of the tokamak wall is an issue to be addressed in the procedures for data analysis. Besides a simple profile fit, a reflection-aware algorithm for tomographic reconstruction is adopted for radiance deconvolution. Results for the neutral flux density distribution at the high-field side (HFS) are presented for low and medium density scenarios, based on the comparison of experimental emission profiles and those obtained by the neutral penetration code KN1D. Absolute values for flux densities at the HFS separatrix are interpreted in terms of SOL parameters and the extension of the plasma-wall gap. A number of examples characterises the D_α video diagnostics as a valuable tool to supply estimates on neutral parameters.

1. Introduction

The scrape-off layer (SOL) and divertor regions are the interface between the core plasma and the material wall of the tokamak. Steady-state operation of a certain discharge scenario is characterized by a circulation of plasma and neutral particles. Losses from the core plasma may be distributed asymmetrically in the poloidal plane, due to the underlying transport parameters. The large values for cross field transport compared to those predicted by neoclassical theory are due to turbulence effects. The dominant parallel field transport results in a distinct pattern of power and particle fluxes to the divertor which is found to be strongly influenced by the configuration of the magnetic field [1, 2]. The main source of neutral particles of the working gas deuterium (or hydrogen) is found in the divertor, fed by the neutralization of ions at the target plates [3] and if low electron temperatures and high densities are present also by volume recombination. The distribution of neutral particles in the SOL is determined by the action of the fundamental reaction mechanisms [4, 5] of molecular dissociation, atomic excitation and ionization and atom-ion charge exchange. The coupling of neutrals to the local ion temperature results in spreading of neutral species beyond the primary origin in the divertor.

Neutrals affect the particle-, momentum- and energy-balance of the plasma in all areas penetrated. The impact of neutrals on the properties of the plasma edge is subject

‡ present address: Leibniz-Institut für Plasmaforschung und Technologie e.V., D-17489 Greifswald, Germany

to many experimental and theoretical investigations. The understanding of the shape of the radial plasma density profile requires the knowledge of transport parameters as well as the source term due to the ionization of neutrals. A common ansatz is to establish a radial expression for the plasma density by the solution of the one dimensional, i.e. radial continuity equation including the ion source term [**?**]. This basic treatment is possible if all parameters are poloidally averaged. The magnitude and radial distribution of transport parameters (convective or diffusive) and neutral density, i.e.penetration depth, are then identified as key parameters. Based on the interconnection of neutrals and the plasma profile shape a relationship of neutral penetration and plasma performance has been proposed. The background is the observation of a correlation between pedestal parameters and global confinement [10] in H-mode discharges. The possible impact of neutral penetration on the magnitude of the H-mode power threshold has also been discussed [11, 12]. Often, parameters of neutrals are deduced from spectroscopic data of a few locations in the SOL according to the diagnostic coverage. In order to compensate the limited experimental access, SOL modelling codes are inferred to bridge the gaps of experimental data. However, the distribution of neutral parameters finally obtained is not necessarily a unique solution, because it is the result of the adaption of several fitting parameters, like local recycling flux and transport coefficients.

The impact of neutrals on the ion velocity distribution at the plasma edge has been treated analytically by several authors. Fülöp et al [13] show that the conventional result for the ion flow velocity obtained in the framework of neoclassial theory is altered if the impact of neutral particles and anomalous effects is considered. It is suggested that anomalous and neutral viscous effects might self-consistently suppress microturbulence by establishing a certain ion flow shear. Similar conclusions are drawn in [14]. Helander et al [15] examined the influence of neutral penetration on the edge plasma rotation where the poloidal distribution of fuelling is considered. In addition to details of the individual approach, the investigations agree in the sense that a key parameter is identified, namely the ratio of neutral to ion density. This ratio is found to be relevant to the edge plasma configuration in a range of $10^{-4} < n_0/n_i < 10^{-3}$. Detailed predictions on neutral-plasma interaction demand experimenal data as a corner stone.

The purpose of this paper is to present the efforts made on the ASDEX Upgrade tokamak to contribute to the topic of neutral particles at the plasma edge by delivering extensive experimental data. For the experiments sketched here, a pair of cameras was operated as video diagnostics to cover large parts of the poloidal cross section. These cameras were equipped with D$_\alpha$ line filters to focus on the emission of excited neutrals in the SOL and near core region. A major complication for data analysis arises from the plasma facing components of ASDEX Upgrade being coated with tungsten. The diffuse reflection impairs the results of standard deconvolution methods.

The paper is devided into the following sections. This introduction is followed by a description of the video diagnostics covering aspects of its assembly and methods used for data deconvolution in section 2. In section 3 the interpretation of emission data by the use of the neutral transport code KN1D is described. The experimental results are presented and discussed in section 4, followed by a summary and concluding remarks in section 5. Appendix A gives a description of the model for diffuse reflection implemented in one of the reconstruction algorithms.

2. Diagnostics and data deconvolution

2.1. Experimental setup and data acquisition

The video diagnostics consists of two channels directed tangentially to the divertor and the midplane. A sketch of the assembly and field of view is shown in figure 1. The optics are installed on an insertion mounting which can be removed from the entry port during baking of the vacuum vessel. The front lens maps the periphery to one end of an image guide, while the other end is mapped to the detector through relay optics containing a narrow filter for the D$_\alpha$ line. With the type of image guides employed ([16]) good image definition can be obtained according to the resolution of the detector of 696×520. The detector is an interline transfer CCD which allows short exposure times of $t_{exp} \gtrsim 20\,\mu s$ at a frame rate of $12\,Hz$.

A prerequisite for data analysis is knowledge of the line of sight geometry. The two main issues are the position of the optical axis and image distortion induced by the lenses employed. An accurate mapping function is constructed using a pin-hole model which is extended by a nonlinear component to mimic the barrel-like distortion observed. A vanishing point is placed close to the actual position of the front lens and the points of intersection of straight lines connecting object point and vanishing point define a 2D image on a mapping plane oriented perpendicularly to the optical axis. The radial distance of image points and optical axis on the projection plane of the linear mapping function is transformed by applying a cubic polynomial. The weighting factors of the quadratic and cubic terms of the polynomial are determined by the analysis of test-patterns. Once the mapping object-to-image plane has been verified (see figure 2), the line of sight geometry for each pixel can be calculated by applying the inverted mapping function.

The diagnostics setup contains some difficulties concerning the issue of radiance calibration. The standard procedure of illuminating the system with a radiance norm (in this case an Ulbricht sphere) is readily done. Although the spectral integration by the setup based on the measured transmission function of the interference filters can be determined, the actual conversion factor of detector response and D$_\alpha$ radiance collected depends on the spectral shape of the D$_\alpha$ profile. The calibration factors $f_{cal,i}$ (to be applied to the raw detector data divided by exposure time) with i identifying a single detector element is

$$f_{cal,i} = \left[\int L_\lambda(\lambda') F_{\lambda,i}(\lambda', \gamma_i) d\lambda' \cdot t_{exp,c} \right] \times$$

$$\left[\left(\frac{\int F_{\lambda,i}(\lambda', \gamma_i) P_{\lambda,i}(\lambda') d\lambda'}{\int P_{\lambda,i}(\lambda') d\lambda'} \right)^{-1} \right] \times \left[(D_{c,i})^{-1} \right] \quad ,$$

where L_λ is the radiance of the calibration light source, F_λ the filter profile which is a function of the pitch angle γ under which light from off axis elements passes the filter, P_λ the spectral profile of the line radiation observed and D_c the detector response to the illumination by the radiance norm. P_λ is mainly determined by Zeeman-splitting and the fraction of hydrogen in the deuterium discharges. For the diagnostics described here, the spectral profile is in fact unknown, because no high resolution spectra were recorded on a viewing geometry comparable to that of the tangential cameras. A high resolution measurement from radially viewing divertor diagnostics was used as a reference to justify the following simplification. To obtain calibration factors, the D$_\alpha$ radiation has been equally weighted in the wavelength interval λ_0 (=656.1 nm) ± 0.1 nm, so a possible contribution of hydrogen has been neglected. In principle also the contribution of Bremsstrahlung needs to be considered. According to the line strength of D$_\alpha$ this is an issue for lines of sight intersecting the core region of high power discharges, in particular with impurity accumulation. For the measurements presented here
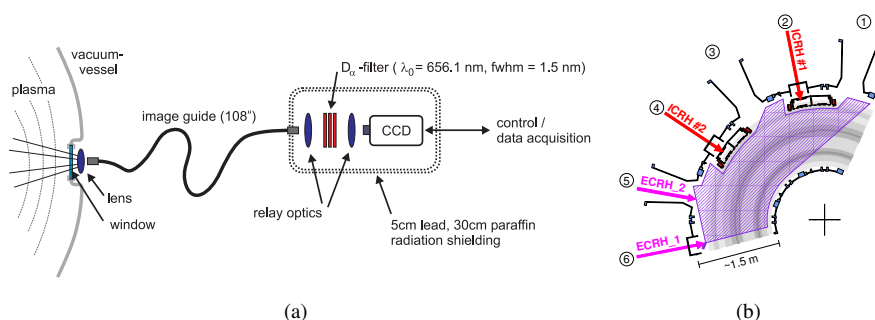
Figure 1. The diagnostics setup (a) and the horizontal cross section of the field of view (b).

this is not the case.

Another important aspect regarding radiance calibration is the sensitivity of the glass made image guides against neutron irradiation. Besides the problem of the transmission of the port window being affected by machine conditioning procedures (e.g. boronization [17]) the image guide transmission plays the major role. In the experimental campaign of the year 2006 with an estimated total neutron production of 10^{18} the transmission of the image guides was observed to degrade to about 10% of its initial value. This behaviour was deduced by analyzing detector response to repeatedly performed standard discharges. For optical diagnostics typically silica fibers are used which are not affected by the level of hard radiation encountered at the ASDEX Upgrade tokamak. The radiation induced damage to silica has been discussed earlier (see e.g. [**?**]) and will be an issue in future devices aiming at D-T operation. In the present case, the reason for the strong degradation of glass is believed to be due to dopands (or impurities) of the fibre material. The elements Ba, Zn, Zr and Pb were detected by proton induced x-ray emission and x-ray flourescence. These heavier elements are more sensitive to ionizing radiation and the colour centers created lead to an attenuation of the passing photon flux. The application of baking procedures to the fibre bundles reveals that the defects can be treated by thermal annealing. Figure 3 shows spectral transmission curves of one image guide sample (length $108''$). Curve I is the absolute spectral transmission of the new sample, curve II shows the result of a transmission measurement after the 2006 experimental campaign with about 500 relevant discharges. The value for transmission at $\lambda \approx 656\,\text{nm}$ is not consistent with the behaviour during the campaign as mentioned above. The illumination during this measurement resulted in photo-bleaching which could clearly be noticed by the naked eye. Baking of the fibre bundle for 24 h at $180°\text{C}$ in a vacuum oven resulted in a recovery of the transmission to the values indicated by curve III. The smaller uncertainty margin for curves II and III are due to an improved setup. As a consequence, short term operation of glass fibres should be preferred. For the data presented in section 4, a systematic uncertainty of the radiance measurement in the range of $\pm 20\%$ is assumed.

2.2. Methods for data deconvolution

The local emission of neutrals ε_{D_α} is obtained by applying inversion algorithms on the radiance data. Two different methods are used. Firstly, in dedicated regions of interest (ROI) with sufficient contrast, a forward fitting procedure based on a model function for
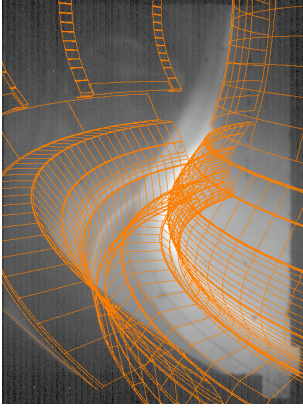
Figure 2. Model of viewing geometry overlayed on D$_\alpha$-image.
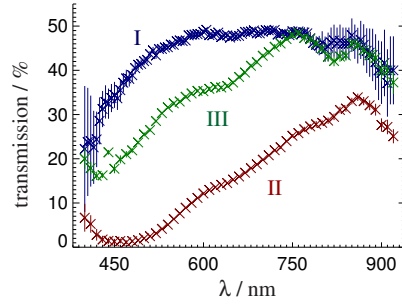
Figure 3. Transmission of the image guide (same sample, different histories); see text.

the radial emission profile is employed. Secondly, data analysis without restrictions on the locations observed is done using an algorithm for tomographic reconstruction which also contains a model for diffuse reflection at tungsten covered plasma facing components (see also Appendix A). Both methods presume toroidal symmetry of emission implying that camera frames containing localized features like gas puffs are not treated.

2.2.1. Profile fit . At some distance from the (lower) X-point along the separatrix ε_{D_α} is present in a rather narrow sheath at the plasma boundary and this nature is also visible in the tangential camera views. Figure 4 shows ROI at the low-field side (LFS) and high-field side (HFS) contained in the two video diagnostics channels which are suitable for a basic approach to data analysis. The idea is to use a simple least-squares fit on the line integrals, where the free parameters are those determining the shape of a radial emission profile. A Lorentzian profile defined on the poloidal magnetic flux label ρ_p has been chosen:

$$\varepsilon_{D_\alpha}(\rho_p) = A \cdot \frac{(w/2)^2}{(\rho_p - \rho_{p,c})^2 + (w/2)^2}(+B) \quad ;$$
$$w = w_i \ , \ \rho_p \leq \rho_{p,c} \quad ; \quad w = w_o \ , \ \rho_p > \rho_{p,c} \quad .$$

Amplitude A, radial centre position $\rho_{p,c}$ and inward and outward decay lengths w_i, w_o are the four free parameters to be adjusted to give a modelled radiance similar to the video data. The offset B is understood not to be part of volume emission of interest, but to represent signal from reflections in the background or even emission in the foreground as is the case for image data of the HFS. The line integrals are obtained numerically by generating a grid along the sightline of each pixel of the ROI. This algorithm is found to converge at the LFS only for image data in front of the carbon tiles (campaign 2006) of the ICRH-antenna limiter frame. The contrast is too low, if tungsten coated components are placed in the background. Since the LFS-ROI is very small, the poloidal variation of the radial emission profile is neglected.

The situation is different for the HFS-ROI. Independent of the type of background components the contrast is sufficient for the forward fitting procedure to be stable. Here, however, the ROI has a considerable vertical extension, such that a poloidal variation of profile parameters needs to be considered. The ROI is separated in practically vertical subsets and for each of those a grid is generated for each pixel containing a radial and a poloidal coordinate. For the latter the *psc* ('poloidal separatrix coordinate') is defined. The *psc* is the distance in
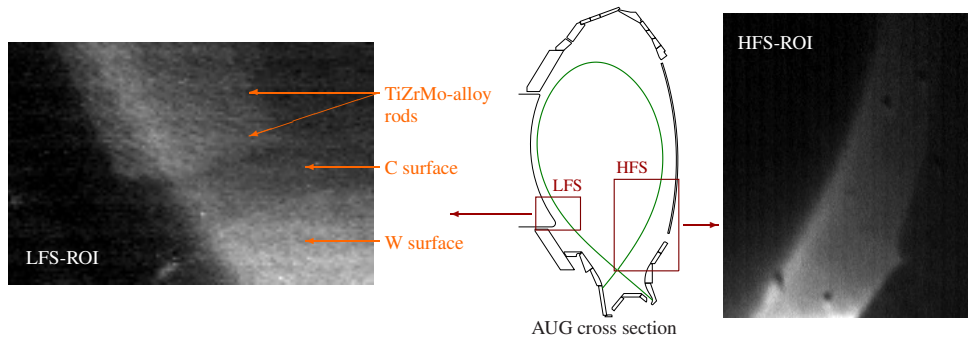
Figure 4. Parts of the frames of both video diagnostics channels and the corresponding positions on the poloidal cross section. The contrast of the LFS-ROI is strongly influenced by components in the background.
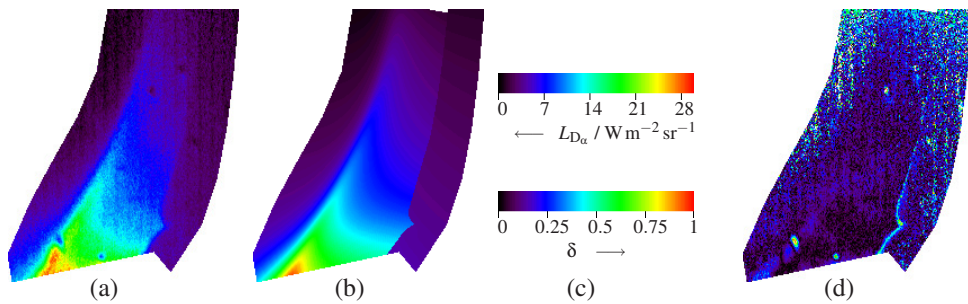
Figure 5. Radiance data of HFS-ROI (a), radiance model (b), deviation δ (d) and corresponding colour scales (c).

the *R*-*z*-plane along the separatrix from the lower X-point to the point on the separatrix which is closest to the grid point of interest. The fitting procedure is performed for each of the subsets separately. Each subset is labelled with a mean *psc*-value which is obtained by averaging the corresponding values of the subset-grids in a radial interval containing the dominant part of the emission sheath. The ROI-subsets are chosen such that *psc*-intervals of about 10 cm result. The fit to the total ROI at first contains unphysical steps in radiance. Basic fit functions are in turn employed on the *psc*-dependence of the profile parameters which can be used to calculate a smooth radiance image. Since both results contain variable settings (*psc*-interval size in the first and type of fit functions in the second step) the emission profiles used for physical interpretation are obtained by using the average profile parameters on each *psc*-interval. The difference of both results is considered as an uncertainty margin for emission. A direct fit of a smooth emission model is impossible due to the instability of an algorithm that contains profile parameters which vary along the lines of sight. The result obtained is exemplified in figure 5. The relative deviation of experimental and modelled radiances are denoted as $\delta = \frac{|L_{model} - L_{exp}|}{L_{exp}}$. In this example, the quality of the model is expressed with the distribution of δ: $\delta \leq 0.25$ for 83 % and $\delta \leq 0.1$ for still 46 % of the data points.

2.2.2. Tomographic reconstruction . When projected to the poloidal plane the lines of sight appear as curves with many crossing points so that the use of a tomographic approach seems promising. The aim is to implement an algorithm which can handle the complete detector data and utilizes the information gathered on the reflection properties of the tungsten coated plasma facing components (Appendix A). The actual tomographic algorithm employed for the deconvolution of tangential camera data belongs to the class of constraint optimizations and was initially developed for the reconstruction of bolometric data [22]. The following optimization problem is formulated:

$$\min \overset{!}{=} \underbrace{\int (div(\mathsf{D}grad\varepsilon))^2 \, dR\, dz}_{\text{regularization constraint}} + A \underbrace{\sum_{\nu=1}^{W} \frac{(\Phi_{\nu,rec} - \Phi_{\nu,meas})^2}{(\delta_\nu \Phi_{\nu,meas})^2}}_{\text{constraint of line integrals}} \equiv T_1 + A \cdot T_2 \quad (1)$$

with ε denoting the unknown emission profile declared on the poloidal plane defined by the variables R and z, D being a weighting tensor, $\Phi_{\nu,rec}$ the line integrals of the reconstructed profile, $\Phi_{\nu,meas}$ and δ_ν the measured data and corresponding relative error, W the number of data points and A a weighting factor used to define the relative contribution of each of the two terms. The second term T_2 is a measure for the quality of the reconstructed ε-profile in terms of line integrals and may be minimized by unphysical profiles. Using the operator $div(\mathsf{D}grad\cdot)$ for the regularization term T_1 implies a large freedom for demanding a certain shape of the profile. The benefit is the direct access to the level of anisotropy with respect to arbitrary directions, which may be a function of the spatial position. This option is used to prefer profile results featuring basic properties of the distribution of emission at the plasma edge, namely the occurrence of large gradients perpendicular and moderate gradients parallel to poloidal magnetic flux (Ψ) surfaces. The shape of the emission profile is governed by the source locations and the mean free path of neutrals which in turn depends on the plasma parameters showing strong perpendicular-Ψ gradients (and parallel-Ψ gradients in the SOL). The weighting tensor D is therefore diagonal on the poloidal magnetic flux topology: $div(\mathsf{D}grad\varepsilon) = div(\mathsf{D}_\perp \vec{n}\vec{n} \cdot \nabla\varepsilon + \mathsf{D}_\parallel \vec{t}\vec{t} \cdot \nabla\varepsilon)$; $\vec{n} = -\nabla\Psi/|\Psi|$; $\vec{t} = \vec{B}_p/|\vec{B}_p|$. The problem (1) is discretized on a rectangular R-z-grid limited by the vessel contour. It can be cast in the form $\iota^T \varepsilon + \varepsilon^T \kappa \varepsilon \overset{!}{=} \min$, where ι and κ are a vector and a matrix, respectively, containing the parameters governed by the line of sight geometry, the magnetic flux topology, the anisotropic weighting tensor D and the weighting factor A. This convex quadratic problem is solved using the NAG routine E04NCF [23] which is an optimization algorithm including linear constraints, here: $0 \leq \varepsilon < \infty$.

At this place, the performance of the algorithm rather than the details of its numerical implementation shall be addressed. To keep the CPU-time within a reasonable limit, the grid resolution is set to $\Delta R = \Delta z = 1$ cm and a detector binning of 3×3 is applied resulting in a grid size of ≈ 9000 and a number of sightlines of about $W \lesssim 25000$ (some regions of the original image of low signal-to-noise ratio are discarded). The flux surface oriented anisotropy of the curvature of ε is imposed by setting $\mathsf{D}_\parallel = 1$ and $\mathsf{D}_\perp = 0.01$. The choice of $\mathsf{D}_\parallel/\mathsf{D}_\perp = 100$ was found to be appropriate for a large amount of data (also different ratios like $\mathsf{D}_\parallel/\mathsf{D}_\perp = 10$ still lead to similar results if the weighting factor A is adjusted accordingly) but, in particular, its assignment to the entire grid is a major simplification. The problem of specifying a reasonable value of $\mathsf{D}_\parallel/\mathsf{D}_\perp$ for each grid point separately is complicated due to the large parameter space and enormous numerical effort for test trials. The quality of the reconstruction algorithm has been examined using a model for the emission profile (see figure 6a) which is oriented on a typical appearence of a low density, lower single null discharge. Phantom detector data is prepared according to a specified viewing geometry and the model for diffuse reflection

presented in the appendix. The line integrals $\Phi_{v,phantom}$ include a primary and secondary part and are implemented as $\Phi_{v,phantom} = \int_{L_1} \varepsilon(l)dl + \sum_{s=1}^{S_{VC}} [\int_{L_2^s} \varepsilon(l)dl \cdot r_s \Delta\Omega_s]$, with l denoting the curve parameter of the sightlines, S_{VC} the number of rays covering the secondary viewing cone, r the solid angle resolved reflectivity and $\Delta\Omega$ the solid angle, respectively. L_1 is the primary sightline and L_2^s are the secondary sightlines of one pixel. The L_2^s are defined by the polar and azimuthal angles b_1^s and b_2^s which cover a viewing cone about the specular primary viewing direction. As the standard setting for the angles b_1^s and b_2^s to ensure a reasonable numerical resolution $\Delta b_1^s = 1°$ and $\Delta b_2^s = 10°$ with $b_1^s \leq 38°$ is chosen. Note that a huge amount of secondary sightlines is created: up to $38 \cdot 36 + 1 = 1369$. The values for the angles required by the reflection model (α, β, γ in the appendix) are obtained by appropriate coordinate transforms following the light path in the reverse direction to that used for the construction of the sightlines.

The reconstruction algorithm does not yield satisfactory results, if the full reflection geometry is implemented at once, because the geometrical definition of sightlines is blurred. The solution to this problem is to perform an iteration on reflection-part reduced input data: the algorithm being aware of primary sightline geometry only is provided with data as would be recorded if the walls were not reflecting, i.e. regarding the reflection part as an undesired offset. The input data to the algorithm read: $\Phi_{v,input}^{(j)} = \Phi_{v,0} - \sum_{s=1}^{S_{VC}} [\int_{L_2^s} \varepsilon^{j-1}(l)dl \cdot r_s \Delta\Omega_s]$,

where j denotes the iteration step, $\Phi_{v,0}$ the original radiance data (experimental or phantom data) and $\Phi_{v,input}^{(0)} \equiv \Phi_{v,0}$ ($\varepsilon^{(-1)}$ undefined). The reconstructed profile is found to converge quickly, such that $j_{max} = 4$ is used.

For running the algorithm, after setting the weighting tensor D and the secondary aperture $b_{1,max}$, merely the weighting factor A remains to be specified. A low value for A corresponds to a strong impact of the regularization term and a smooth profile is obtained. Setting A to large values gives a more accurate match of line-integrals, but also leads to unphysically sharp and scattered profiles. The profile reconstruction from phantom data reveals that a global minimum for the profile deviation exists. In the real application, only the match of line integrals can be used as a criterion. This is found to exhibit a $1/A$ behaviour with the best profile match in the model case for A in the transition region of extreme slopes, as might have been expected from the two-term ansatz. The final result is chosen from a confidence interval of about $A \pm 20\%$, because no exact criterion exists. It is important to mention that the results of this confidence interval are very similar and the level of deviations is irrelevant in the framework of interpretation described in this paper.

Figure 6 shows the reconstructed profiles with and without the consideration of diffuse reflection. The benefit of the secondary viewing geometry is the reduction of artefacts, the most obvious being located on top of the divertor roof baffle. Stability of the algorithm concerning phantom data is found for $b_{1,max} \leq 25°$ while for experimental data $b_{1,max} = 38°$ can be set. The phantom data has been deconvoluted using the exactly matching viewing geometry and without consideration of noise. In the case of experimental data one has to take into account that viewing geometry and model for diffuse reflectivity are both approximations. It is important to note that this algorithm tends to indicate emission in the X-point region which is not contained in the model. However, the main features at the HFS are resolved. Because the spatial resolution of the tomographic reconstruction is low compared to the profile fit described in preceding section and artefacts are not completely suppressed, this algorithm is employed to give a more qualitative overview on the emission profile in the divertor region. The main features like the occurrence of separate emission maxima at the
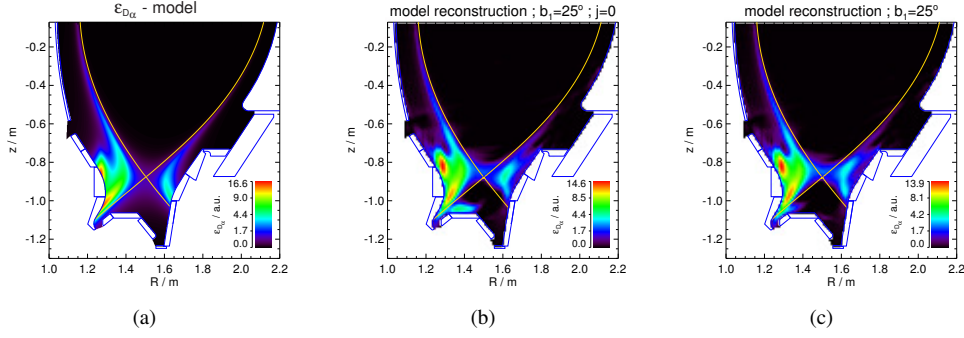
Figure 6. Profile model (a) to provide phantom data, profile reconstruction without (b) and with (c) the consideration of diffuse reflection.

HFS are nevertheless resolved and may give valuable hints on the underlying plasma and neutral parameters.

3. Emission and neutral parameters

The D$_\alpha$-radiation is emitted from excited atomic deuterium. This excited species is generated in several reactions, including dissociative excitation of molecules (D$_2$) and molecular ions (D$_2^+$), direct excitation of atomic deuterium or radiative recombination of atomic ions and electrons. The emission profile is determined by the local densities of the involved neutral species, the plasma parameters and the related photon emissivity coefficients. In this work the radial evolution of neutral parameters is modelled employing the kinetic neutral transport code KN1D [24]. The experimental emission profile is used as a criterion to set the free (or uncertain) parameters of the code.

A complete description of the code KN1D is given in the reference. Here merely the details needed to judge the results presented in section 4 are summarized. KN1D solves the coupled Boltzmann equations for molecular and atomic hydrogen in an ionizing plasma on a 1D geometry related to the situation found at the plasma edge in magnetic confinement devices. From the resulting velocity distribution functions, all moments of interest can be calculated. The main input parameters are the grid geometry (range of coordinate x), plasma parameters (n_e, T_e, T_i) on the grid and the molecular flux density at the grid boundary far from the plasma. It is important to note that this scheme of analysis is not self-consistent, since the plasma background is fixed and independent from the magnitude of neutral flux imposed. According to the ROI on the radiance diagnostics, typical KN1D grid lines as shown in figure 7a are constructed. The grid boundaries in the SOL are the vessel wall at the HFS and a position at a distance of 20 cm from the separatrix at the LFS which is in the limiter shadow of a large entry port. The grid boundaries in the core region are chosen such that the assumption of zero neutral flux in the opposite direction (i.e. to the vessel wall) is fulfilled. Profiles of plasma density at the LFS are provided by integrated data analysis including lithium beam excitation spectroscopy and laser interferometry [25]. T_e profiles are obtained by combining results from the electron cyclotron emission diagnostics and defining an exponential decay length in the SOL such that a reasonable shape of $\varepsilon_{D_\alpha}(x)$ (see figure 7b) results. Accurate measurements in the LFS-SOL for T_e are not available for the discharges discussed in section 4. For the grids at the HFS data from the LFS core is mapped according to the poloidal

magnetic flux contours, but for the SOL both n_e and T_e are described by exponential decay lengths, since this region is not covered by plasma diagnostics. The assumptions for T_e on the LFS and n_e and T_e at the HFS are indeed strong - therefore large uncertainty margins have been considered, ranging from 30% (40%) in the SOL to 10% (20%) in the core region for n_e (T_e). Based on these uncertainties, the extreme profile values are combined to four different pairs as input sets for KN1D. Those sets are used to gather some information on the resulting uncertainty concerning the neutral data and is presented in the form of error bars in the plots. The ion temperature which is not routinely available from diagnostics, is always set to twice the electron temperature, due to the lack of better knowledge, but hints from experimental and modelling results (see e.g. [26]). However, T_i was not found to influence the resulting neutral parameters considerably in a range of about T_i=1-3$\times T_e$ in dedicated test runs. The free parameter of neutral molecular flux density at the grid boundary is determined by an iteration on the matching criterion, which is the value of the radially (i.e. along the *x*-grid) integrated emission. The reference $\varepsilon_{D_\alpha}(x)$ profile based on the code results is calculated by multiplying the molecular and atomic densities by the electron density and the related photon emissivity coefficients taken from the ADAS database [27] for molecular dissociative and atomic excitation, respectively. In fact, the contribution of dissociative excitation is very small, accounting for a few per cent in the SOL in the present cases. The density of D_2^+ is very low and therefore it is not considered for the calculation of $\varepsilon_{D_\alpha}(x)$, the relatively high rate coefficient for dissociative excitation of the molecular ion already taken into account. Also, radiative recombination can be neglected, because none of the cases examined here exhibits large plasma densities in combination with low electron temperatures ($T_e \lesssim 1$ eV).

Typical results of this procedure are shown in figures 7b and 7c. The abscissae of these plots display the 1D-grid of the kinetic code and are labelled relative to the separatrix position 'x_{sep}'. Because of the definition of decay lengths for both n_e and T_e in the HFS-SOL, the interpretation of radiance data is much more difficult in this area. At the HFS the KN1D runs are started at those positions far from the lower X-point (large 'psc') and for the definition of the decay lengths on all grids a monotonic behaviour towards the divertor is assumed. The cases labelled 'L' and 'H' are discharges of similar line averaged density of $\overline{n_e} = 5 \cdot 10^{19}$ m^{-3} with L- and H-mode like edge density profiles, respectively. Figure 8 shows the atomic neutral density profiles at the LFS obtained by the KN1D model matching the D$_\alpha$ diagnostics data. The plots merely exemplify the procedure of data analysis and a dedicated discussion of experimental data is given in the following section.

4. Results and discussion

A selection of frames and discharges is shown which is believed to characterize the D$_\alpha$ video diagnostics so as to make a valuable contribution to the understanding of edge and SOL properties. To be able to compare the different scenarios (shot number and time slice) presented, a number of rather global plasma parameters is specified. These are the line averaged density in the midplane $\overline{n_e}$, heating power (ohmic and auxiliary) P_{heat}, MHD energy content W_{MHD} and a confinement factor denoted as H_{89} according to the ITER89-P scaling [28]. For the discussion on neutral flux densities the data from ionization gauges below the divertor roof baffle or the lower heatshield are useful, denoted as $\Gamma_{D,div}^G$ and $\Gamma_{D,lhs}^G$, respectively. If not stated otherwise, diagnostics data on the edge profile such as n_e and T_e are time averaged with respect to the interval of exposure time of the video diagnostics frames.
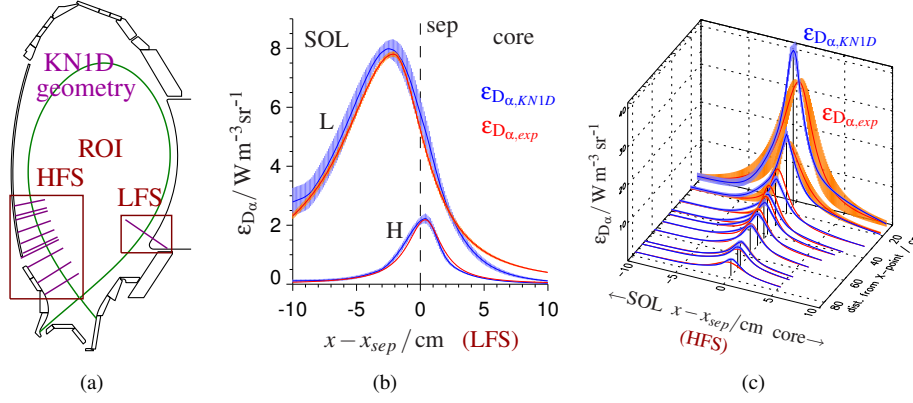
Figure 7. KN1D grid lines on the poloidal cross section (a). Comparison of experimental and modelled ε_{D_α} profiles at the LFS for two different cases ('L','H') (b) and at the HFS (c).
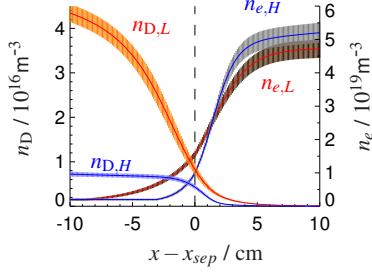

Figure 8. Electron and atomic neutral density profiles corresponding to $\varepsilon_{D_\alpha}(x)$ data of figure 7b.

4.1. Regime change in L-mode

The low density L-mode discharge #21418 was run in the framework of core turbulence studies. It contained a phase of electron cyclotron resonance heating (ECRH) applied at two power levels. In addition to the changes of core characteristics the confinement properties were altered and gave a useful example of the sensitivity of the D$_\alpha$ diagnostics. The fundamental parameters of the two time slices shown here are for $t_1 \approx 2.3$ s: $\overline{n_e} = 3.4 \cdot 10^{19}\,\text{m}^{-3}$, $P_{heat} = 700$ kW, $W_{\text{MHD}} = 130$ kJ, $H_{89}=1.3$ and for $t_2 \approx 3.4$ s: $\overline{n_e} = 3.65 \cdot 10^{19}\text{m}^{-3}$, $P_{heat} = 850$ kW, $W_{\text{MHD}} = 190$ kJ, $H_{89}=1.8$. Available gauge measurements read for t_1: $\Gamma_{\text{D},div}^{\text{G}} = 1.4 \cdot 10^{22}\text{m}^{-2}\text{s}^{-1}$, $\Gamma_{\text{D},lhs}^{\text{G}} = 3.5 \cdot 10^{21}\text{m}^{-2}\text{s}^{-1}$ and for t_2: $\Gamma_{\text{D},div}^{\text{G}} = 1.2 \cdot 10^{22}\text{m}^{-2}\text{s}^{-1}$, $\Gamma_{\text{D},lhs}^{\text{G}} = 2.7 \cdot 10^{21}\text{m}^{-2}\text{s}^{-1}$.

Time traces of $\overline{n_e}$, ECRH power level and gas feed are depicted in figure 9. At the step of ECRH at $t = 3$ s the particle confinement is enhanced, seen in the rise in $\overline{n_e}$. Since $\overline{n_e}$ is feedback controlled, the gas feed is switched off. In this figure the bars denoted as t_1 and t_2 indicate the time intervals in which D$_\alpha$ data of the LFS has been averaged (several frames each). This was done to assure that the observed radial shift of the ε_{D_α} profile in the order of 5 mm is a robust finding. The corresponding ion source profiles S$_{D+}$ together with n_e are shown in figure 10a. With a lower particle confinement during t_1, both the ion source and density profile are larger in the SOL, indicating an increased recycling flux. The profiles of T_e are shown in figure 10b - note that the SOL part is estimated. Even in this case of relatively small changes in the plasma edge configuration, the D$_\alpha$ diagnostics does not only deliver estimates on neutral parameters, but is also a relevant reference for density and temperature
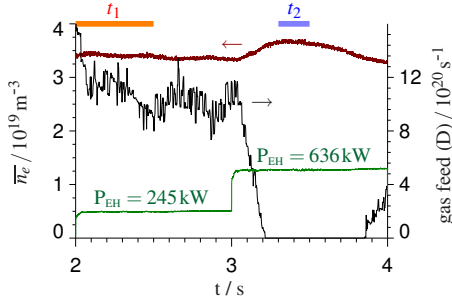
Figure 9. Time traces of #21418 for $\overline{n_e}$, ECRH power level and gas feed. The intervals t_1 and t_2 relate to the frames of D$_\alpha$ data examined.

diagnostics, since the parameters are interconnected.

The 2D emission profiles from tomographic reconstruction of two camera frames of the divertor view are shown in figures 11a and 11b. The emission at the LFS wall at $z = -0.4$ m and above the X-point appear in every reconstructed profile and are considered to be artefacts, because both features are incompatible with the radiance images. A major difference in the emission pattern is observed at the HFS target. During t_1 the peak emission is at the inner strike point and in the region above, whereas in t_2 the emission above the target is less pronounced. The more detailed analysis of the HFS-ROI in terms of neutral flux densities is shown in figures 12a and 12b. This clearly confirms the expectation that the neutral flux density is largest near the divertor. Compared to the value found for the LFS-ROI it is suspected that the lower HFS is the dominant region in terms of core fuelling in contrast to a sometimes suggested X-point fuelling.

The level of agreement with respect to the equivalent atomic neutral flux density at the wall ($2 \cdot \Gamma_{D_2,wall}$) from the gauge measurement as stated above is moderate. At similar vertical positions a discrepancy of a factor of about 3 is observed. Changes in the SOL parameters which only marginally influence the emission profile to be compatible with the camera data and the simplification of the 1D treatment (radial penetration) for the torus shaped plasma chamber are found to only have a rather small impact on $\Gamma_{D_2,wall}$ in the order of 10 %. It is suspected that the $\parallel \vec{B}$ plasma flow towards the divertor acts as to confine neutrals in the divertor region partly by radiationless reactions like elastic collisions or charge exchange reactions. Since such a preferential direction is not contained in the simplified KN1D geometry, less neutrals starting from the wall are required in the 1D code to produce a certain emission profile at the plasma edge. However, even when relating to the basic KN1D picture it is apparent from the comparison of particle fluxes at wall and separatrix that a large fraction of the initial neutral flux is lost by ionization in the SOL (~ 75 %) before the core plasma is reached.

Compared to the values at t_1, the appearance of Γ_{D,sep,HFS,t_2} might indicate that more neutrals escape the divertor region (lower flux density closer to X-point) and reach locations further upstream (comparable flux further upstream, although the total flux during t_2 is lower). With the flux values for HFS and LFS of figure 12b a rough estimate on the core fuelling rate $F_{D,core}$ can be made. Considering the area of the separatrix surface at the HFS on the *psc*-interval covered and at the LFS of $\Delta psc = 0.5$ m per definition the lower bounds (concerning the total core fuelling) are: $F_{D,core,HFS,t_1} \approx 2.1 \cdot 10^{21}\,\text{s}^{-1}$, $F_{D,core,LFS,t_1} \approx 5.3 \cdot 10^{20}\,\text{s}^{-1}$, $F_{D,core,HFS,t_2} \approx 1.8 \cdot 10^{21}\,\text{s}^{-1}$, $F_{D,core,LFS,t_2} \approx 4.2 \cdot 10^{20}\,\text{s}^{-1}$.
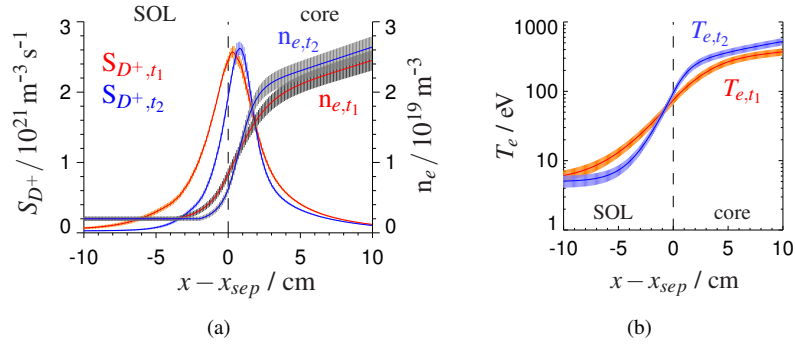
Figure 10. Profiles of ion source term and electron density (a) and of electron temperature (b) on the LFS during the time slices t_1 and t_2 of #21418.
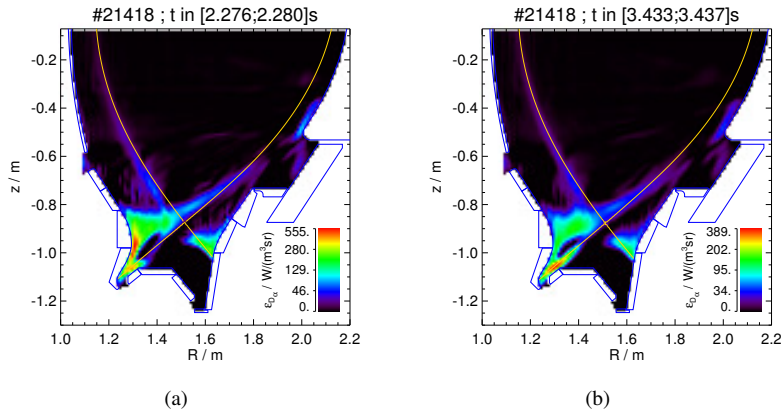
Figure 11. D$_\alpha$ emission profiles of #21418 at t_1 (a) and t_2 (b).
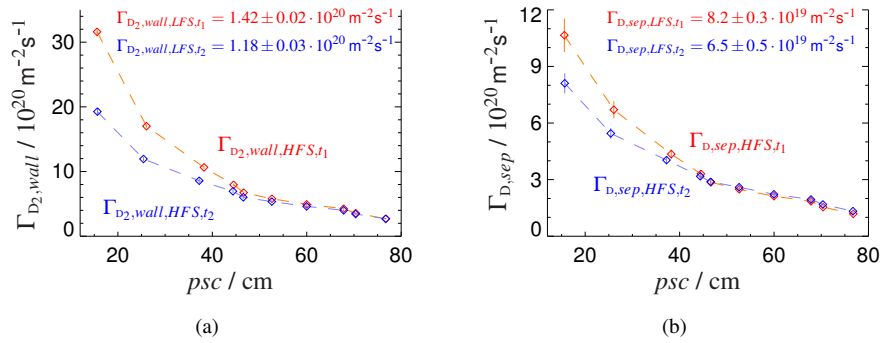
**Figure 12.** Neutral flux density at HFS wall (a) and at the HFS separatrix (b) of #21418 at t_1, t_2.

4.2. Impact of inner wall gap on HFS fuelling

Discharge #22097 belongs to a series in which the impact of geometry parameters such as inner and outer wall gap and position of the lower X-point on the appearence of D$_\alpha$ emission was examined. One of these is presented here focussing on the separation between the wall and the separatrix at the HFS. The global reference parameters of the two time slices shown are for $t_1 \approx 3.1$ s: $\overline{n_e} = 5.4 \cdot 10^{19}$ m^{-3}, $P_{heat} = 2.0$ MW, $R_{out} = 2.11$ m, $R_{in} = 1.11$ m, H$_{89}$=1.8 and for $t_2 \approx 3.7$ s: $\overline{n_e} = 4.1 \cdot 10^{19}$ m^{-3}, $P_{heat} = 2.1$ MW, $R_{out} = 2.15$ m, $R_{in} = 1.14$ m, H$_{89}$=1.6. R_{out} and R_{in} denote the radial positions of the separatrix in the midplane obtained from MHD equilibrium reconstruction. Available gauge measurements read for t_1: $\Gamma_{\mathrm{D},div}^{\mathrm{G}} = 6.6 \cdot 10^{21}$ m^{-2}s^{-1}, $\Gamma_{\mathrm{D},lhs}^{\mathrm{G}} = 2.0 \cdot 10^{21}$ m^{-2}s^{-1} and for t_2: $\Gamma_{\mathrm{D},div}^{\mathrm{G}} = 6.8 \cdot 10^{21}$ m^{-2}s^{-1}, $\Gamma_{\mathrm{D},lhs}^{\mathrm{G}} = 1.7 \cdot 10^{21}$ m^{-2}s^{-1}.

Figure 15 shows time traces of $\overline{n_e}$, auxiliary heating power, gas feed and radial position. The discharge was configured to contain phases of ohmic and ECR heating, both at two radial positions of the plasma column. t_1 and t_2 belong to the ECRH phase and are more H-mode like scenarios. At the beginning of the ECRH phase, $\overline{n_e}$ rises strongly and the gas feed is switched off according to density feedback control. The interesting feature of this configuration is that $\overline{n_e}$ shows a pronounced reaction on the radial shift of the plasma by ~ 3 cm, although the level of heating power is unchanged. Since the elevation of $\overline{n_e}$ during the phase of ECRH and smaller R_{in} is about 25% it is speculated that the confinement properties of the discharge are indeed not only influenced by the level of heating power but also by the radial position, because it seems unlikely that the additional particle content could be found in the HFS-SOL entirely. If the confinement properties are not different, then for t_1 the losses from the core are recycled more efficiently than for t_2, i.e. less plasma flux reaches the divertor region where the neutrals are pumped. It is important to note that the geometrical settings used here are well within the standard margins of the plasma control scheme and do not represent extreme configurations.

The emission profiles are depicted in figures 13a and 13b. Both profiles are similar in magnitude but the inner strike point is hidden at t_1. The power level is the same for both times and the gauge measurements indicate only a slightly lower neutral divertor flux for t_1 than for t_2. With a similar particle flux it is suspected that the temperature at the inner target is lower such that the emissivity coefficient would drop significantly. According to the gauge data from the lower heatshield and the flux density at the separatrix shown in figure 14 a larger fraction of SOL plasma flux is recycled at the inner wall during t_1 than t_2. This might imply a reduced power flux to the inner target and could explain the shape of the $\varepsilon_{\mathrm{D}_\alpha}$ profile. During t_2 the profile of the flux distribution is slightly tilted with a larger contribution at higher *psc*. During the phase of larger wall gap, neutrals may penetrate more freely in the vertical direction, presumed that the radial SOL decay length are similar for the two time intervals. The corresponding core fuelling rates in this *psc*-interval are the same: $F_{\mathrm{D},core} \approx 3.3 \cdot 10^{20}$ s^{-1}. To maintain the higher $\overline{n_e}$ at t_1 there must be other contributions to the core fuelling rate not covered with the measurements presented here. The upper part of the heatshield could be one candidate, but the standard video diagnostics (system with low dynamic range not described here) did not show pronounced plasma recycling in that region.

This example shows that there are contributions to the SOL fluxes which have a rather large radial excursion such that small changes in the radial position of the plasma column can have an impact on the recycling pattern and particle content of the discharge.

#22097 ; t in [3.060,3.061]s

#22097 ; t in [3.740,3.741]s

(a)   (b)
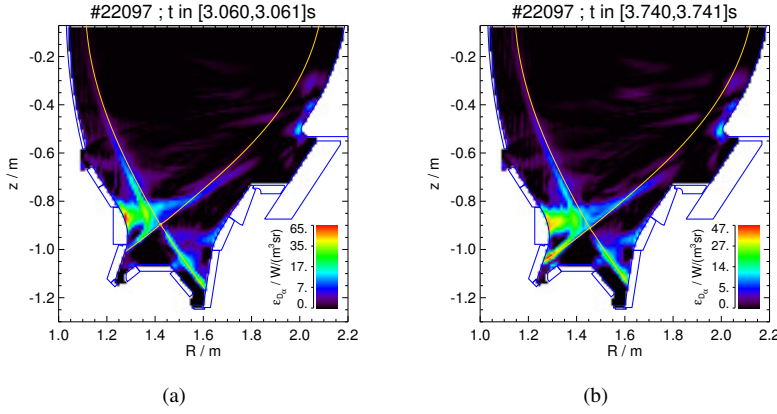
Figure 13. D_α emission profiles of #22097 at t_1 (a) and t_2 (b).
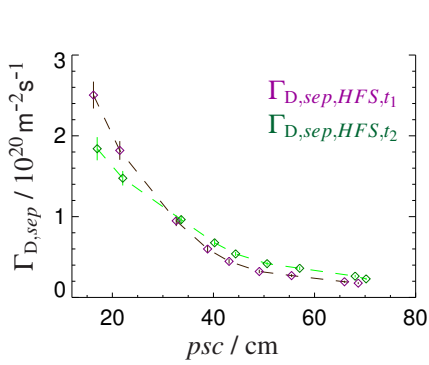
Figure 14. Neutral flux density at the HFS separatrix of #22097 at t_1, t_2.
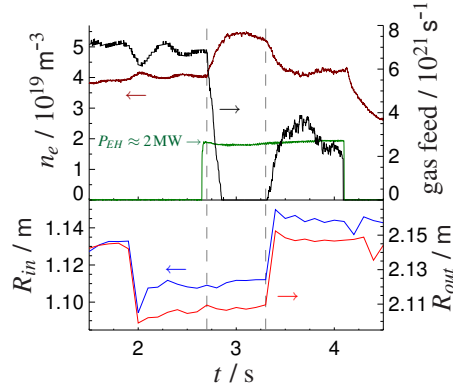
Figure 15. Time traces of parameters related to particle content (top) and radial position (bottom) for #22097.

4.3. Limitations and problems

When trying to analyze D_α radiance data from arbitrary plasma scenarios it becomes apparent that the procedures sketched in sections 2.2 and 3 are applicable only to a limited subset due to several restrictions. Those are briefly mentioned in the following.

For the profile fit to converge at the LFS, a sufficient contrast in the radiance data is mandatory. One of the main conditions aside from the plasma edge configuration itself is a plain and dark background. For the diagnostics presented in this paper it is the surface coating of an ICRH limiter frame tile which is decisive for the data analysis to be successful. Convergence was found if the tile was plain graphite whereas no results could be obtained for the tungsten covered tile (the tiles where changed in the framework of the tungsten programme [34]). Reflections from regions of large emission such as the divertor region blur the image obtained for the LFS-ROI.

The issue of contrast mentioned above is also related to the radial density gradients and the magnitude of divertor fluxes. For low and medium density discharges up to

$\overline{n_e} = 5 \cdot 10^{19}\,\mathrm{m^{-3}}$ usually both data from the HFS-ROI and the divertor region can be analyzed. The contrast is highest for H-mode like scenarios where the density gradients are larger at the edge and the density in the SOL is lower compared to L-mode discharges. The observed ε_{D_α} is located in a rather narrow sheath close to the separatrix. For L-mode conditions the core density must be lower to still obtain sufficient contrast in the midplane. In the picture of D$_\alpha$ radiance the divertor region is often found to be uniformly highlighted in L-mode, except for low density ohmic conditions. In the case of uniform distributions of emission in the divertor, the settings for the algorithm of tomographic reconstruction stated in 2.2 are not appropriate. The weighting tensor D must be chosen so as to obtain more isotropic distributions. In high density H-mode discharges the appearence of D$_\alpha$ radiance gradually evolves into a situation in which no valuable information can be gathered from the video diagnostics. With the higher density in the SOL and the corresponding larger ionization rate the plasma and neutral fluxes in the SOL increase nonlinearly with the line averaged density and ε_{D_α} profiles become very broad. In addition, the radiation from the divertor region dominates the scene and the plasma vessel is illuminated entirely thereby diminishing every detail except for the strike zones.

A third aspect relates to the assumption of toroidal symmetry of ε_{D_α}. Localized emission due to gas puffs or limiter glow obviously violates the precondition for data analysis but can be avoided rather easily. The problem to be addressed here is the question whether the deduced radial distribution of ε_{D_α} is actually a time average of emission patterns of distinct structures such as filaments. H-mode scenarios are often accompanied with frequent edge perturbations, summarised under the term edge localized mode (ELM) which can transport several per cent of the stored energy in burst like events from the core to the divertor [29]. The locally increased electron temperature and/or density result in an elevated ε_{D_α} in filamentary structures and can be observed by fast optical diagnostics [30]. The standard method for ELM detection is the recording of the periodic modulation of divertor radiation, e.g. by fast photo diodes directed towards the target plates. According to this time trace diagnostics data are often sorted with respect to inter-ELM phases. This can be done equally for the video diagnostics, but the radiance data indicate that this procedure might not be safe. Firstly, the transport time of the perturbation from the midplane to the divertor needs to be taken into account and secondly, it was found that filamentary structures can be observed without the occurrence of a signature in the divertor. The latter aspect is based on radiance data recorded at short exposure times, e.g. $t_{exp} = 20\,\mu$s, which can be set for the interline-transfer CCD. Although the frame rate is very low ($\sim 12\,\mathrm{Hz}$), the comparison of consecutive frames reveals the presence of filamentary structures. The important aspect is that these structures can - besides H-modes - also be observed in some L-mode discharges, but without a periodic modulation of divertor radiation. Images from the divertor view indicate that the plasma in these structures is lost to the LFS wall before reaching the divertor due to a large radial excursion. So the presence of edge turbulence seems not generally to induce varying divertor plasma parameters. This topic cannot be treated accurately by the slow video system used here, but two statements are made to stress this issue. In an ELMy scenario, the basic analysis for the LFS-ROI gives radial profiles with a radial jitter in the order on a cm for a series of frames in an otherwise 'steady state'. The discharges discussed in this paper are characterized by calm edge conditions which has to be regarded as a claim without proof. The low to medium density discharges showed no divertor modulation and gave no jitter for the LFS-profiles, but the exposure times had to be set to relatively large values $t_{exp} \geq 10\,\mathrm{ms}$ in order to achieve a sufficient signal-to-noise ratio.

5. Summary and conclusion

At the ASDEX Upgrade tokamak two tangentially viewing cameras were installed in the 2006 and 2007 experimental campaigns as to deduce parameters of neutrals from D$_\alpha$ radiance data. The video diagnostics system has been absolutely calibrated and two methods for data analysis were implemented. A basic forward profile fit was used to obtain emission profiles at the LFS and HFS. For data of the divertor view an algorithm for tomographic reconstruction has been employed which was extended by a model for diffuse reflection obtained experimentally. The latter was found to be mandatory for visible light tomography in an all-tungsten machine.

The data presented for neutral flux densities on the LFS and HFS are based on a comparison of the 1D neutral penetration code KN1D and the experimental emission profiles. Flux density distributions of atomic deuterium at the lower heatshield were presented and discussed for low and medium density scenarios. The lower HFS is found to be the main fuelling location and the distribution of neutrals there and in the divertor is influenced by the gap between the plasma column and the inner wall even at relatively large separations. A typical observation is that about a quarter of the neutral wall flux reaches the separatrix. The tomographic reconstruction shows a second pronounced emission zone above the inner strike zone which can surpass the latter and is interpreted in terms of SOL fluxes with larger radial excursion.

The methods for data deconvolution and interpretation contain several assumptions and problems which reveal that the accuracy of D$_\alpha$ diagnostics is limited. On the one hand, interpretation on the HFS relies on estimates of plasma parameters in the SOL. On the other hand, absolute values for neutral density and flux density are in reasonable agreement with gauge measurements. Additionaly, the neutral parameters at the separatrix cannot be supplied by any other diagnostics.

Focusing on the tomographic reconstruction of video data, the poloidal distribution of D$_\alpha$ emission may be considered as a benchmark criterion for complex self-consistent modelling codes like SOLPS [31]. The benefit of the video diagnostics is that a large fraction of the poloidal cross section is covered in contrast to other localized diagnostics which are positioned in the LFS midplane or at the target plates. For next step devices such as ITER, in particular those plasma scenarios are of interest which finally offer the desired fusion performance. For high density and high recycling regimes the D$_\alpha$ video diagnostics unfortunately cannot resolve local emission due to the problems described in section 4.3. However, the construction of the plasma and neutral grids of SOLPS does not account for the relationship between position of the plasma column and the recycling pattern. The size of the plasma grid is limited due to the condition that a connection must exist between inner and outer target. Ions are reflected as neutrals from the plasma grid boundary and SOL plasma flows which result in emission patterns above the inner strike point cannot be modelled appropriately. It is the opinion of the author that this issue should be resolved prior to the application of codes like SOLPS in the ITER design process. In this field, data like obtained with D$_\alpha$ video diagnostics could be of value.

Several aspects on the video diagnostics concerning implementation, data analysis and experimental results could be sketched only briefly to catch the main issues. For a more detailed view on the topic the reader may refer to [32].

Appendix A. Reflection properties of tungsten surfaces

At the AUG tokamak, a stepwise transition of the first wall from carbon to tungsten has been pursued over several experimental campaigns. An elaborate discussion of this tungsten

programme can be found in [33, 34]. The presence of metallic surfaces in the plasma vessel displays a drawback for diagnostics in the visible spectral range, because reflected light might be part of the detected signal. A detailed knowledge of the reflection properties is required to judge the relevance of this issue for a particular diagnostic application. Here, the construction of a model for diffuse reflection to be applied in D$_\alpha$ video diagnostics data analysis is briefly sketched. In this section, the solid angle resolved reflectivity is denoted as r, while the total, i.e. solid angle integrated, reflectivity is denoted as R.

Figure A1 shows the experimental setup. An original and clean divertor tile has been used for the reflectivity measurement. The light source is an optical parametric oscillator (OPO, $\lambda \approx 656.1\,\mathrm{nm}$). Two photodiodes (A and B in figure A1) are used to record the intensities of the incident and the scattered beam, respectively. Grey filters of defined attenuation are introduced to operate the diodes around the optimum working point to achieve good S/N-R and to avoid saturation. Additional D$_\alpha$-filters are used to exlude the recording of stray light from the pump laser or idler radiation of the OPO. The noise level of the detector signals and uncertainties concerning the transmission of the grey filters are considered when deducing the magnitude of reflection from the diodes response.

The test sample is mounted on a rotary table placed in the beam path such that the angle of incidence α can be adjusted easily. A goniometric mounting which allows us to set turn and pitch angles β and γ is placed in the direction of specular reflection. The vertex of the cone to be probed coincides with the point of light incidence at the surface of the sample. A small tube which is blackened on the inside is used to define the aperture of the reflection viewing geometry.

A few examples for measurement series are depicted in figure A2a. Corresponding to the mechanical setup, the angle of incidence is restricted to $\alpha \in [30, 85]^\circ$ and the polar angle $\gamma \leq 38^\circ$. The three parameters α, β and γ have been chosen from the sets $\alpha \in \{30, 37.5, 45, 52.5, 60, 67.5, 75, 80, 85\}^\circ$, $\beta \in [0, 180]^\circ$ ($\Delta\beta = 15^\circ$) and $\gamma \in \{0., 2.5, 5, 10, 15, 20, 25, 30, 35, 38\}^\circ$. The range of β was fixed after the first series supported the assumption of symmetry about the plane of incidence within the margin of uncertainty. All possible combinations of the three angles, if applicable in the present setup, were examined, just for the two largest values of α only the zero order direction was measured, resulting in a total number of 768 single measurements for the construction of a model of diffuse reflectivity. As indicated in figure A2(a) basic trigonometric functions have been used to interpolate the experimental data. Linear interpolation schemes are applied for arbitrary (α, β, γ)-triplets in the α-interval covered by the measurements. No data are available for $\alpha < 30^\circ$ and the model is extrapolated by applying the result for $\alpha = 30^\circ$ which is found not to contain a β-dependence. Extrapolation for $\alpha > 75^\circ$ is based on the two remaining values for reflection in the zero order direction and a dependence on γ is introduced to achieve a reasonable value for total reflectivity which must not exceed unity. The solid angle integrated reflectivity, where $\gamma \leq 38^\circ$, is shown in figure A2(b). Figure A3 gives a three dimensional depiction of the reflectivity model with colour coding on the surface of a sphere centred at the point of incidence. One interesting feature of the observed reflectivity (in this particular case) is the deviation of the peak value from the specular direction which is tilted towards the surface normal by several degrees. The accuracy of the goniometric setup is sufficient to exclude a systematic error in that respect.

In addition to the limitations of the reflectivity model due to the mechanical constraints of the experimental setup, it should be mentioned that the examined tile represents only one specific configuration. A look into the plasma vessel after plasma exposure reveals that in fact every single point at the first wall exhibits an individual character of reflectivity. Compared to the original tile, there are, on the one hand, areas which appear more 'shiny'
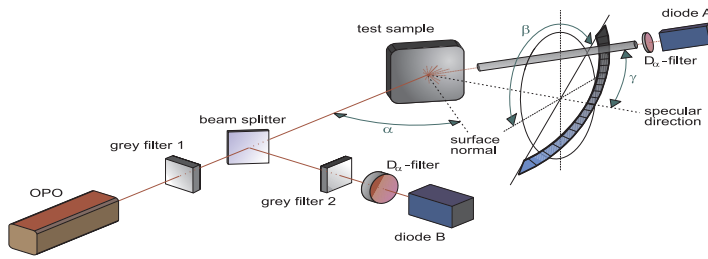
Figure A1. Scheme of the setup to measure diffuse reflectivity, solid angle resolved.
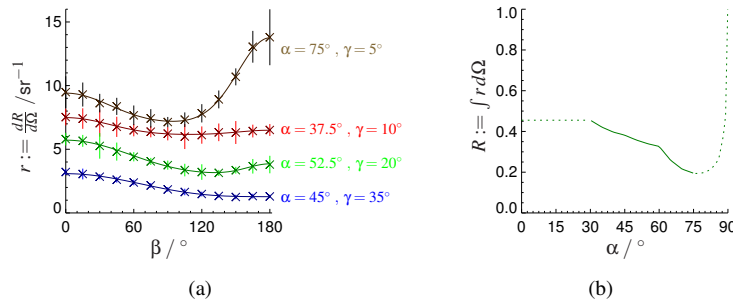

Figure A2. *r*-series on β for fixed α and γ (a) and total reflectivity R of the *r*-model (b) ($\gamma \leq 38°$), measured (solid), extrapolated (dotted).

probably due to a reduction of the surface roughness by plasma treatment. On the other hand, shadowed areas are covered with layers - either from eroded material released at other locations or deposits from wall conditioning procedures - which can result in reduced reflectivity or even show pronounced interference effects. Consequently, the model presented here cannot cover all aspects of the real situation, but rather has to be regarded as a pragmatic approach. Nevertheless, this model is believed to be much more relevant for data analysis than a simplified treatment using e.g. reflection coefficients for specular geometry only.

References

[1] LaBombard B *et al* 2004 *Nucl. Fusion* **44** 1047-66
[2] Asakura N, ITPA SOL and Divertor Topical Group 2007 *J. Nucl. Mater.* **363-365** 41-51
[3] Mertens Ph, Brezinsek S, Greenland P T, Hey J D, Pospieszczyk A, Reiter D, Samm U, Schweer B, Sergienko G and Vietzke E 2001 *Plasma Phys. Control. Fusion* **43** A349-73
[4] Harrison M F A 1985 *Atomic and Molecular Collisions in the Plasma Boundary* CLM-P746 UKAEA Culham Laboratory, Abingdon
[5] Janev R K, Langer W D, Evans K Jr and Post D E Jr 1987 *Elementary Processes in Hydrogen-Helium Plasmas* (Berlin: Springer)
[6] Boivin R L *et al* 2000 *Phys. Plasmas* **7** (5) 1919-26
[7] Groebner R J, Mahdavi M A, Leonard A W, Osborne T H and Porter G 2002 *Plasma Phys. Control. Fusion* **44** A265-72
[8] Mahdavi M A, Maingi R, Groebner R J, Leonard A W, Osborne T H and Porter G 2003 *Phys. Plasmas* **10** (10) 3984-91
[9] Kallenbach A, Asakura N, Kirk A, Korotkov A, Mahdavi M A, Mossessian D and Porter G 2005 *J. Nucl. Mater.* **337-339** 381-85
[10] Osborne T H, Groebner R J, Lao L L, Leonard A W, Maingi R, Miller R L, Porter G D, Thomas D M and Waltz R E 1998 *Plasma Phys. Control. Fusion* **40** 845-50
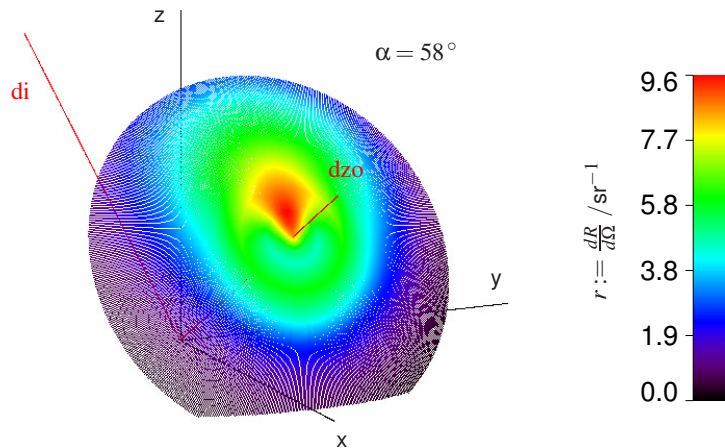
Figure A3. $r(\alpha = 58°, \beta, \gamma)$ colour coded on spherical surface centred at point of incidence. Surface coordinate system (x,y,z), with z-axis denoting the surface normal. Direction of incidence 'di' and direction of zero order 'dzo' in x-z-plane.

[11] Tsuchiya K, Takenaga H, Fukuda T, Kamada Y, Ishida S, Sato M, Takizuka T and the JT-60 Team 1996 *Plasma Phys. Control. Fusion* **38** 1295-99

[12] Owen L W, Carreras B A, Maingi R, Mioduszewski P K, Carlstrom T N and Groebner R J 1998 *Plasma Phys. Control. Fusion* **40** 717-20

[13] Fülöp T, Catto P J and Helander P 1998 *Phys. Plasmas* **5** 3969-73

[14] Catto P J, Helander P, Connor J W and Hazeltine R D 1998 *Phys. Plasmas* **5** 3961-68

[15] Helander P, Fülöp T and Catto P J 2003 *Phys. Plasmas* **10** 4396-404

[16] http://www.us.schott.com/lightingimaging/english/products/healthcare/imagingfiberoptics/flexiblecomponents/wound.html

[17] Winter J 1996 *Plasma Phys. Control. Fusion* **38** 1503-42

[18] Friebele E J, Askins C G, Gingerich M E and Long K J 1984 *Nucl. Instrum. Methods Phys. Res. B* **1** 355-69

[19] Ramsey A T and Hill K W 1992 *Rev. Sci. Instrum.* **63** 4735-37

[20] Ramsey A T, Tighe W, Bartolick J and Morgan P D 1997 *Rev. Sci. Instrum.* **68** 632-35

[21] Ramsey A T 1995 *Rev. Sci. Instrum.* **66** 871-76

[22] Fuchs J C, Mast K F, Herrmann A, Lackner K, ASDEX Upgrade-, NBI- and ICRH-Teams 1994 *Proc. 21th EPS Conf. on Controlled Fusion and Plasma Physics (Montpellier)* vol 18B part III ed Joffrin E *et al* (Geneva: EPS) pp 1308-11

[23] http://www.nag.com/numeric/fl/manual20/pdf/E04/e04ncf.pdf

[24] KN1D code, http://www.psfc.mit.edu/̃labombard/KN1D_Source_Info.html

[25] Fischer R, Wolfrum E, Schweinzer J and the ASDEX Upgrade Team 2008 *Plasma Phys. Control. Fusion* **50** 085009

[26] Chankin A V *et al* 2006 *Plasma Phys. Control. Fusion* **48** 839-68

[27] ADAS - Atomic Data and Analysis Structure, http://adas.phys.strath.ac.uk

[28] Yushmanov P N, Takizuka T, Riedel K S, Kardaun O J W F, Cordey J G, Kaye S M and Post D E 1990 *Nucl. Fusion* **30** 1999-2006

[29] Leonard A W *et al* 1999 *J. Nuc. Mat.* **266-269** 109-17

[30] Koch B *et al* 2007 *J. Nuc. Mat.* **363-365** 1056-60

[31] Schneider R, Coster D, Braams B, Xantopoulos P, Rozhansky V, Voskoboynikov S, Kovaltsova L and Bürbaumer H 2000 *Contrib. Plasma Phys.* **40** 328-33

[32] http://edoc.ub.uni-muenchen.de/10034

[33] Neu R 2003 *Tungsten as a Plasma Facing Material in Fusion Devices* IPP 10/25 (Garching: Max-Planck-Institut für Plasmaphysik)

[34] Neu R *et al* 2007 *Plasma Phys. Control. Fusion* **49** B59-70